crystals

MDPI

Article

Tungsten Bronze-Type Ceramics for Temperature-Stable Energy Storage Properties: A Feasibility Study

Xi Shi * and Neamul H. Khansur *

Department of Materials Science and Engineering, Friedrich-Alexander-University Erlangen-Nürnberg (FAU), 91058 Erlangen, Germany

* Correspondence: xi.shi@fau.de (X.S.); neamul.khansur@fau.de (N.H.K.)

Abstract: The temperature-dependent energy storage properties of four tungsten bronze-type ceramics are studied together with an investigation of their structure and temperature-dependent permittivity response, i.e., $Ba_6Ti_2Nb_8O_{30}$ (BTN), $Ba_6Zr_2Nb_8O_{30}$ (BZN), $Sr_3TiNb_4O_{15}$ (STN) and $Sr_3ZrNb_4O_{15}$ (SZN) ceramics. With different cations at A and B sites, those four ceramics exhibit different crystal structures and show significantly different microstructure features and dielectric responses with changing temperatures. It was observed under SEM that BZN has smaller grains and a more porous structure than BTN. SZN shows the most porous structure among all samples, exhibiting a much lower permittivity response than other samples with no signs of phase transitions from room temperature to 400 °C. Though the energy storage response of those samples is generally quite low, they exhibit good temperature stability together with low dielectric loss. It was suggested that by obtaining a denser structure through chemical modification or other methods, those tungsten bronze ceramics with good temperature stability could be promising as energy storage devices when improved energy storage properties are achieved.

Keywords: energy storage properties; tungsten bronze-type ceramics; porous ceramics

Citation: Shi, X.; Khansur, N.H. Tungsten Bronze-Type Ceramics for Temperature-Stable Energy Storage Properties: A Feasibility Study. *Crystals* **2023**, *13*, 1073. https://doi.org/10.3390/cryst13071073

Academic Editors: Haibo Zhang, Dawei Wang, Hana Uršič and Alexander Martin

Received: 13 June 2023
Revised: 4 July 2023
Accepted: 7 July 2023
Published: 8 July 2023

1. Introduction

Dielectric ceramic capacitors show high power density (~10^8 W/kg), fast charge-discharging rate (<1 μs), and good thermal stability, therefore are crucial as energy storage devices in applications such as pulse power industries, medical equipment, and electronic devices [1], etc. Among those dielectric ceramic capacitors, relaxor ferroelectrics show better energy storage properties (such as recoverable energy storage density, W_{rec}, and energy efficiency, η) than ferroelectrics and paraelectric materials due to the higher maximum polarization, lower energy loss, and higher breakdown field attributed from their unique microstructure with polar nano regions [1]. The typical material systems include $PbZrO_3$-based and lead-free perovskite-structured systems including $BaTiO_3$ (BT)-based, $K_{0.5}Na_{0.5}NbO_3$ (KNN)-based, and $Na_{1/2}Bi_{1/2}TiO_3$ (NBT)-based ceramics. Since the usage of lead is restricted due to its toxicity to the environment, research is intensively focused on developing promising lead-free systems, and great research advances have been achieved. For example, a high W_{rec} of 1.76 J/cm^3 was reported in $0.94Bi_{0.55}Na_{0.45}TiO_3$-$0.06BaTiO_3$ ceramics under 75 kV/cm [2], BT based $0.7BT$-$0.3BiScO_3$ ceramics obtained a W_{rec} of 2.3 J/cm^3 under 225 kV/cm [3], 0.85KNN-0.15ST showed a W_{rec} of 4.03 J/cm^3 under 400 kV/cm [4].

Tetragonal tungsten bronze (TTB) structure with polar distortion is one of the major categories of lead-free ferroelectrics [5–8]. Over recent years, TTB ferroelectrics have been researched due to their excellent non-linear optic, pyroelectric, and optoelectronic properties [9,10]. In the meantime, tetragonal tungsten bronze (TTB) structured materials could also be potential energy storage materials, such as $Sr_{1-x}Ba_xNb_2O_6$ (SBN), $Ba_{6-3x}Nd_{8+2x}Ti_{18}O_{54}$ (BNT), $Ba_6Ti_2Nb_8O_{30}$ (BTN), $Sr_3TiNb_4O_{15}$ (STN). They have a general formula $(A1)_2(A2)_4(C)_4(B1)_2(B2)_8O_{30}$. A1 represents a 12-coordinate site, A2 is a

15-coordinate site, and B1 and B2 are 6-coordinate octahedral sites [11]. Smaller triangular (C) sites could be (partially) filled by small low-charged cations which are generally empty, therefore the formula becomes $A_6B_{10}O_{30}$. TTB materials are normally porous due to the abnormal grain growth during sintering [12] and the properties would greatly vary when different elements are located at A, B, and C sites, allowing the manipulation of their structure and properties [13]. TTB ceramics with a relaxor ferroelectric nature are especially attractive as energy storage devices. For example, Fe-doped tungsten bronze $Sr_{1-x}Ba_xNb_2O_6$ (SBN) ceramics could achieve W_{rec} of 0.68 J/cm^3 and η of 83.6% [14]. MgO-$Sr_{0.7}Ba_{0.3}Nb_2O_6$ composites show W_{rec} of 0.93 J/cm^3 together with η of 89.4%. The $(Sr_{0.7}Ba_{0.3})_5LaNb_7Ti_3O_{30}$ tungsten bronze ceramic was reported to have a W_{rec} of 1.36 J/cm^3 and η of 91.9% [6].

$Ba_6Ti_2Nb_8O_{30}$ (BTN) ceramic was first reported in 1965 [15]. It has a tetragonal structure (space group *P4bm*), with lattice parameters a = b = 12.53 Å and c = 4.01 Å (See Figure S1 in Supplementary Materials for structure information). The structure consists of NbO_6 octahedra sharing corners occupied by Nb and Ti forming two main interstices (A1 and A2) [16]. Both pentagonal A1-sites and tetragonal A2-sites are predominantly occupied by Ba. The co-existence of pentagonal and tetragonal sites results in trigonal vacant C-sites [16]. BTN ceramic was initially studied as a ferroelectric due to its low dielectric loss and low-temperature coefficient of relative permittivity [17,18]. It was reported that its electrical properties are preferable when sintering in a reducing atmosphere leading to more electrons generated together with oxygen vacancies [19]. $Sr_3TiNb_4O_{15}$ (STN) tungsten bronze phase has been recently determined to have an orthorhombic structure with unit cell a = 12.363 Å, b = 12.4 Å, and c = 7.76 Å [11,20], different from BTN. It is suggested the smaller ionic radius of Sr^{2+} compared to Ba^{2+} allows for more flexibility in the structure leading to this orthorhombic structure [21]. Pure STN is known to show low conductivity and owns a relaxor nature due to the composition disorder at A and B sites with Curie temperature at around 600 °C [22]. Unfortunately, there is a lack of fundamental understanding of those materials as well as their performance as potential energy storage devices.

In this work, we have looked into the structural features and small signal dielectric properties of four representative tungsten bronze ceramics, i.e., $Ba_6Ti_2Nb_8O_{30}$ (BTN), $Ba_6Zr_2Nb_8O_{30}$ (BZN), $Sr_3TiNb_4O_{15}$ (STN), $Sr_3ZrNb_4O_{15}$ (SZN) ceramics as well as systematically studied their energy storage properties at different temperatures, which could provide insights for implementing them as temperature stable energy storage devices, provided with improved energy storage response.

2. Methodology

$Ba_6Ti_2Nb_8O_{30}$ (BTN), $Ba_6Zr_2Nb_8O_{30}$ (BZN), $Sr_3TiNb_4O_{15}$ (STN), $Sr_3ZrNb_4O_{15}$ (SZN) tungsten bronze ceramics were fabricated using the conventional solid-state reaction method using high-purity reagent powders in stoichiometric ratios: $BaCO_3$ (Sigma Aldrich, St. Louis, MI, USA, 99.9%), TiO_2 (Sigma Aldrich, 99.9%), Nb_2O_5 (Sigma Aldrich, 99.99%), $SrCO_3$ (Sigma Aldrich, 99.9%) and ZrO_2 (Sigma Aldrich, 99%). The mixed powders for each composition were milled by planetary milling (Pulverisette 5, Fritsch GmbH, Idar-Oberstein, Germany) using zirconia balls and ethanol as milling media in polyamide milling containers for 24 h at 250 RPM. Then the powders were calcined at 950 °C in air for 42 h and milled again for 24 h at 250 RPM using ethanol and zirconia balls. The dried powder after the second milling was uniaxially pressed and cold isostatically pressed at 190 MPa for 3 min. Afterward, the pellet-shaped samples were sintered at 1300 °C for 7 days in air.

X-ray diffraction (XRD) patterns were collected from the ground sample surfaces using a Bruker D8 Advance diffractometer (Bruker AXS GmbH, Karlsruhe, Germany). The XRD data was processed through the Rietveld refinement method by TOPAS software. The instrumental peak shapes for XRD data were optimized with respect to Al_2O_3 data using the fundamental parameter approach in TOPAS. The background was fitted with

Chebychev polynomial function. Beyond that phase-specific peak broadening parameters were refined to account for crystallite size and microstrain effects. The microstructure of mirror-polished, thermally etched (1200 °C, air, 1 h) samples was examined under a scanning electron microscope (SEM) (Quanta 200, FEI Co., Ltd., Hillsboro, OR, USA). The relative permittivity was measured with an LCR meter (E4980AL, Keysight, Santa Rosa, CA, USA) from room temperature to 400 °C with 2 K/min heating/cooling rate on samples with Pt electrodes (Balzers SCD040) on both sides. The energy storage property test at different temperatures is based on measuring the polarization-electric field (PE) loops of the samples (around 0.5 mm thick). Before measurement, the ground samples were annealed in air at 500 °C for 1 h to remove the stress effects from mechanical processing and then sputtered with Pt electrodes at both sides. The tests were performed with a maximum field of 140 kV/cm with a unipolar waveform under a frequency of 100 Hz on a TF Analyser 2000 (aixACCT (aixPES), Aachen, Germany). Samples were immersed in insulating silicon oil (Wacker®-AP 100 Silicone Fluid) during the tests.

3. Results and Discussion

The X-ray diffraction (XRD) patterns shown in Figure 1a indicate that both BTN ($Ba_6Ti_2Nb_8O_{30}$) [16] and BZN ($Ba_6Zr_2Nb_8O_{30}$) [13] have a tetragonal structure with the space group *P4bm*. For BTN, it appears no secondary phase within the resolution limit of the instrument, based on the Rietveld refinement (see Figure 1b), unlike previous studies where the secondary phase such as $Ba_3Ti_4Nb_4O_{21}$ appears [19,23]. It was found in a study that the sintering aid MnO would facilitate forming a single-phase BTN which could probably act as nucleation sites [23]. The Rietveld refinement results for the other three samples can be found in Text S3 of Supplementary Materials. BZN has the same structure as BTN and is also a relaxor ferroelectric with the equal-valence B-site substitution of Zr^{4+} for Ti^{4+} [13]. The reflections of BZN at around 29.43°, 39.47°, and 43.18° correspond to the secondary phase $Ba_5Nb_4O_{15}$ (Space group $P\bar{3}m1$, a = 5.741 Å and c = 11.572 Å), of which the phase fraction is calculated to be approximately 6% based on the Rietveld refinement (see Figure S3a of Supplementary Materials). As the $Sr_3Ti_{1-x}Zr_xNb_4O_{15}$ (STZN) compound, the Ti-rich end member $Sr_3TiNb_4O_{15}$ (STN) (x = 0.0) has a orthorhombic structure with $Pna2_1$ symmetry (a = 12.378 Å, b = 12.363 Å, c = 7.795 Å) [11]. The minor peak at around 29.49° is unidentified (see Figure S3b in Supplementary Materials). The SZN end member (x = 1.0) has the same crystal symmetry as STN despite being substituted with larger cations of Zr^{4+} (radius 0.72 Å) instead of Ti^{4+} (radius 0.605 Å), consistent with the earlier study [11] (Lattice parameters are a = 12.176 Å, b = 12.434 Å, and c = 7.756 Å). Based on the Rietveld refinement, SZN did not show any significant amount of secondary phase (see Figure S3d).

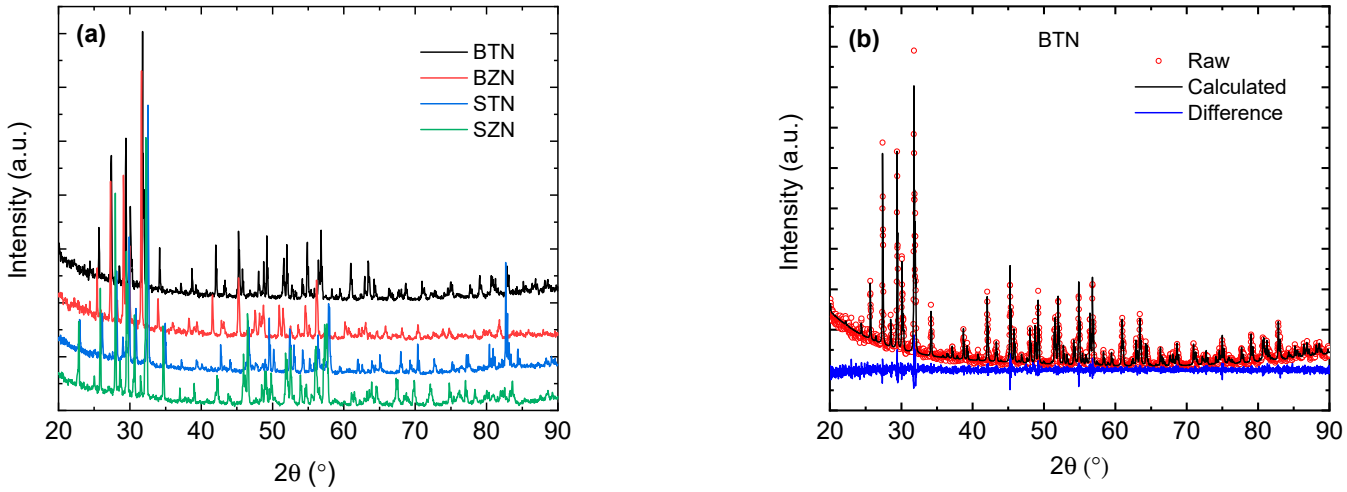

Figure 1. Normalized XRD patterns of BTN, BZN, STN and SZN at room temperature between 20° and 90° (**a**); Rietveld refinement of BTN data (**b**).

Figure 2 shows the microstructure features of the surfaces of the as-sintered samples under SEM. It is seen that they all have a porous structure with different extents of apparent porosity. In Figure 2a, BTN shows big equiaxed grains with an average grain size of 10 μm and round-shaped grains with an average grain size of 5 μm (from Energy Dispersive Spectroscopy (EDS) analysis it is known the grains with different shapes have the same composition, see Text S2 in Supplementary Materials), consistent with earlier studies [16]. Among the four samples, BZN has the smallest grains (size of around 1–2 μm) and an intergranular array of pores and grains (Figure 2b), in agreement with a previous study [13]. Compared with other samples, STN has quite inhomogeneous grain sizes with extra big grains (e.g., around 40 μm in size) (Figure 2c), as well as fewer pores. In contrast, SZN is most porous with connected irregular grains [13], which could influence its permittivity response and energy storage properties. Based on Archimedes' principle, the apparent porosity is estimated to be 2.44%, 2.27%, 1.61%, and 6.35% for BTN, BZN, STN, and SZN respectively, in agreement with the microstructure features shown in Figure 2 where SZN has the more porous structure and STN has the densest structure. It is suggested the intensively distributed pores and unclear grain boundaries in those samples (especially in BZN and SZN) are due to the release of CO_2 gas during the fabrication process, resulting in low sample density [13]. It was reported in another study that using MnO as a sintering aid could wet the grain boundary and increase the diffusion rate, resulting in a denser structure with fewer pores [23]. EDS analysis (see Figure S2 and Table S1 in Supplementary Materials) confirmed that the chemical compositions of the four samples are successfully achieved without any contamination, despite a minor secondary phase in BZN and probably also in STN.

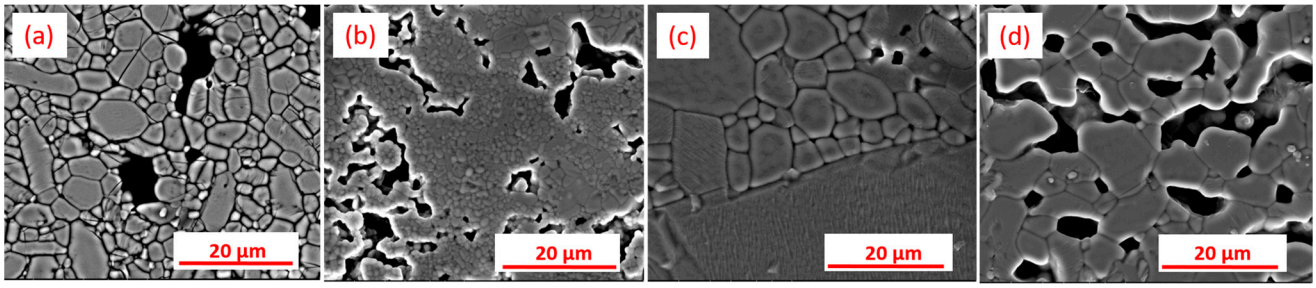

Figure 2. Microstructure images of (**a**) BTN; (**b**) BZN; (**c**) STN; and (**d**) SZN ceramic samples.

Figure 3 shows the temperature-dependent permittivity of the four TTB samples. Except for SZN which has a rather low relative permittivity (<150) which is probably associated with its porous structure (see Figure 2d), the maximum permittivity of other samples is all above 1000.

The transition at around 200 °C in BTN and 150 °C for STN (See Figure 3a,c) indicates ferroelectric to paraelectric transition across Curie temperature, in agreement with previous works [22,24]. Also, it is noted that this transition is broadened, possibly arising from the order-disorder variations of TiO_6 and NbO_6 for BTN and STN [25]. It has been reported that the diffuse exponent, γ, of STN and BTN is 1.41, and 1.95 respectively (when $\gamma = 1$, its fits the behavior for normal ferroelectric ceramic, when $\gamma = 2$, it fits the typical relaxor behavior) [25]. This type of diffused ferroelectric nature was also seen in other TTB ceramics [26,27]. It is also seen that the dielectric loss of BTN and STN show a sudden increase from 200–250 °C together with the corresponding permittivity. Based on similar studies it can be concluded the corresponding peaks are not signals of transitions [11,25]. Instead, it could be due to the motion of charge carriers including oxygen vacancies which are thermally activated at higher temperatures, with higher conductivity for samples [28]. Also, the increased dielectric loss could arise from the reduced contribution of ferroelectric domain walls at high temperatures [29]. Nevertheless, all samples have a rather low dielectric loss (less than 0.4 at frequencies above 1 kHz) till 400 °C, indicating great potential in electronic applications, in agreement with other similar studies on TTB compounds [11,27].

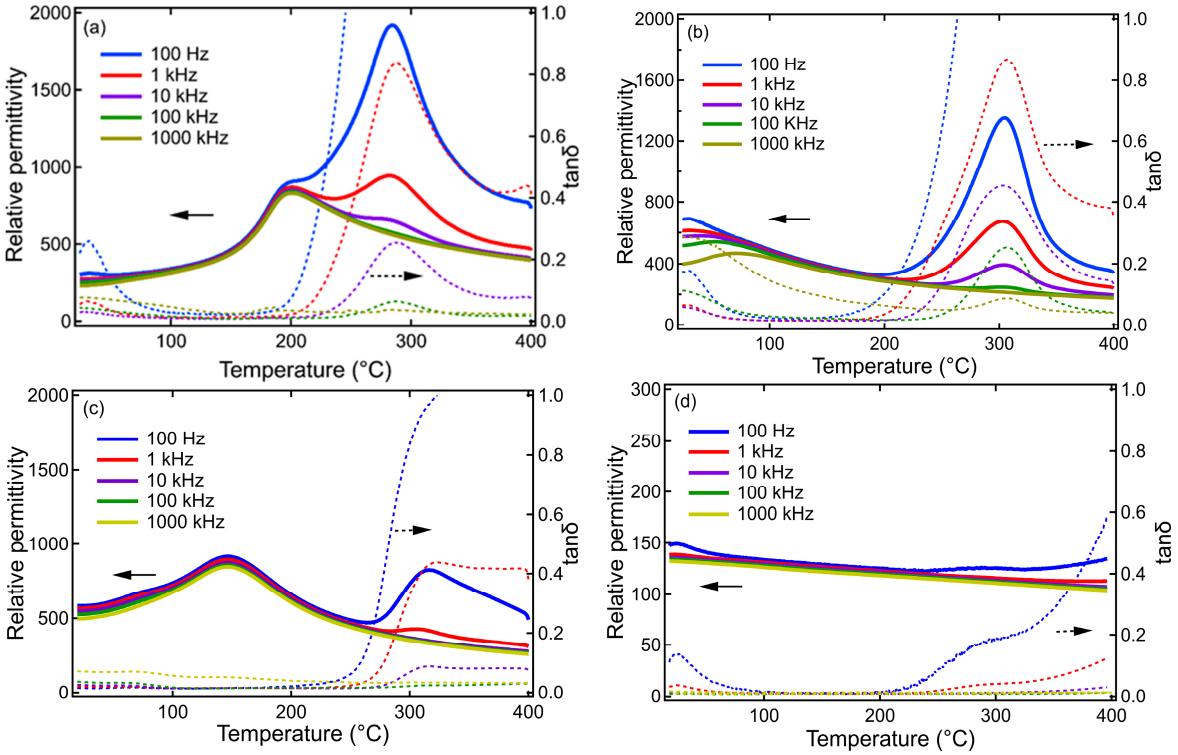

Figure 3. Temperature-dependent permittivity of BTN (**a**); BZN (**b**); STN (**c**) and SZN (**d**) (heating round) at different frequencies between room temperature and 400 °C.

In Figure 3b, BZN seems to show the strongest relaxor behavior among all samples, showing strong frequency dependence in permittivity and loss tanδ, where the permittivity peaks move to higher temperatures with increasing frequency. In a similar study for porous BZN, the maximum permittivity also occurs around room temperature with strong frequency dispersion and γ reaches 1.87 [13]. Similar to BTN and SZN, the permittivity and dielectric loss of BZN significantly increase from 200 °C and then decline at 300 °C. The corresponding peak at 300 °C could be associated with the dynamics of polar nano regions in this relaxor composition [13] or space charge effects.

Interestingly, SZN shows stable permittivity and dielectric loss values with increasing temperature, indicating no phase or structural transitions in this range (Figure 3d). SZN could be ferroelectric with small domains or only piezoelectric [11]. Another study [11] suggested that there is a phase transition for SZN at 500 °C. Compared with STN, the shift of phase transitions to higher temperatures in SZN leads to more stable piezoelectric properties in this wide temperature range [11].

Figure 4a,b show the temperature-dependent P(E) loops of BZN and STN samples under the maximum electric field of 140 kV/cm and 100 kV/cm, respectively. The maximum polarization (P_{max}) for BZN is below 6 μC/cm^2 under 140 kV/cm and below 8 μC/cm^2 for STN under 100 kV/cm. With temperature, the maximum polarization shows a slight decline for both samples. It is also found that the remanent polarization (P_r) gets larger and the P(E) loop becomes lossy at higher temperatures. The highest endurable electric field for BZN and STN samples is 140 and 120 kV/cm. BZN has a more porous structure than STN, as shown in Figure 2. Pores would reduce the effective field applied on the sample, so the porous BZN can sustain a higher field [13] than STN with a denser microstructure. As seen in Figure 4c, the W_{rec} for both samples is less than 1 μC/cm^3, which is rather low to serve as energy storage materials. A similar energy storage response is also observed for the other two compositions, i.e., BTN and SZN (the data for BTN and SZN are not shown due to lack of complete data at all temperatures). At room temperature, the W_{rec} of BZN at 140 KV/cm is 0.29 J/cm^3 and shows a minor decline with temperature till 0.17 J/cm^3

at 150 °C due to increased conductivity. In contrast, STN shows a similar W_{rec} at room temperature at 100 kV/cm with a slightly increased energy storage response at 150 °C of 0.29 J/cm^3 due to reduced energy loss. The η (%) shows a similar trend as W_{rec} for both BZN and STN respectively. In Figure 4d, it declines significantly from around 80% to 39%, due to the increased conductivity with the sample with temperature for BZN, while for STN it overall increases from 70% to 79% from room temperature to 150 °C.

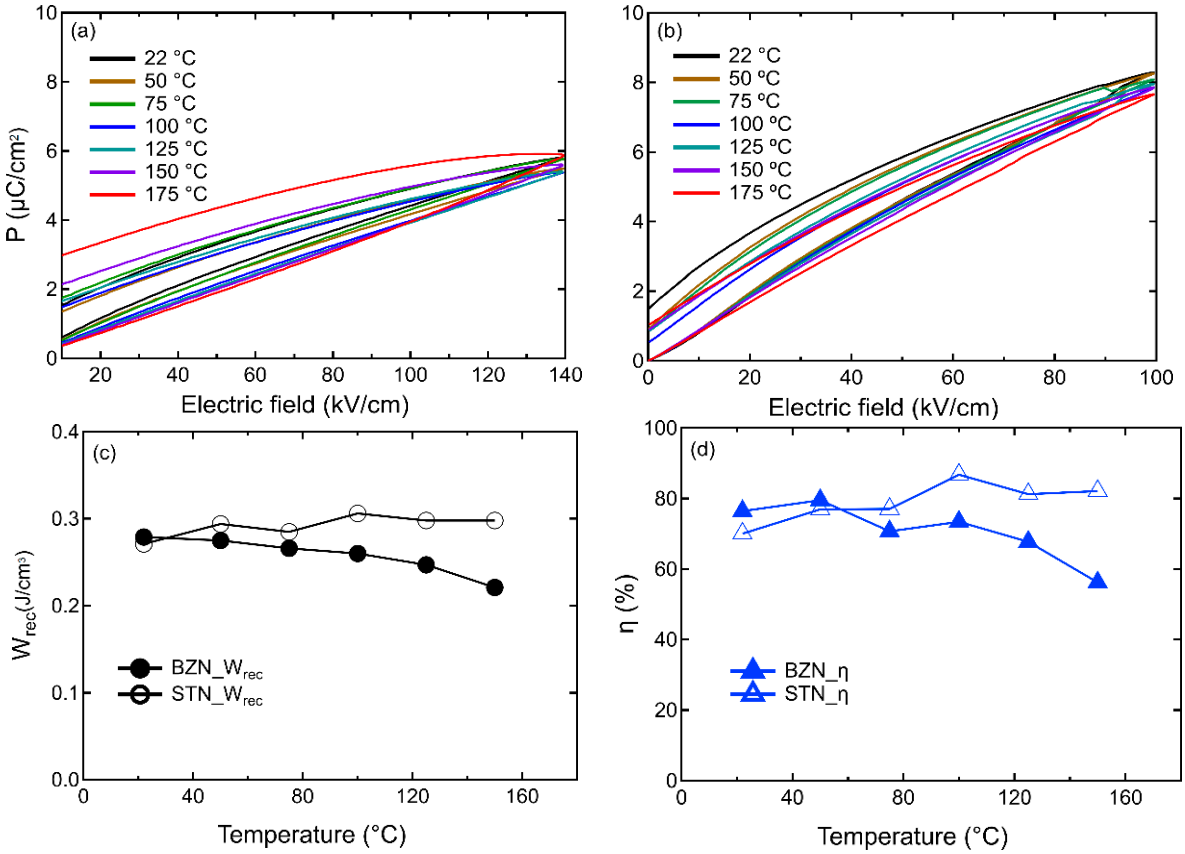

Figure 4. Temperature-dependent electric field-polarization loops of BZN (**a**) and STN (**b**) from room temperature to 175 °C under the electric field of 140 kV/cm and 100 kV/cm respectively; calculated recoverable energy density (W_{rec}) and energy storage efficiency (η) from room temperature to 150 °C for BZN (**c**) and STN (**d**).

The porous structure of those TTB samples could lead to a low breakdown field and therefore limit their energy storage response, as shown in Figure 4. Those energy storage properties could be potentially improved by chemical doping. For example, B site Ta-doped $Sr_2NaNb_{3.5}Ta_{1.5}O_{15}$ shows an increased breakdown strength and improved energy density of 3.99 J/cm^3 and η of 91.7% [30]. Sb-doped $Sr_2Na_{0.8}Ag_{0.2}Nb_{4.7}Sb_{0.3}O_{15}$ tungsten bronze ceramics show enhanced relaxor nature and could achieve W_{rec} of 2.27 J/cm^3 and η of 93.3% [31]. Those doped samples show dense microstructure and no abnormal growth crystal grains. Similar enhanced relaxor nature and energy storage properties are also seen in other ceramics such as Sb-modified $(Sr_{0.515}Ba_{0.47}Gd_{0.01})$ $(Nb_{1.9-x}Ta_{0.1}Sb_x)O_6$ (SBGNT) based ceramics [32], CuO-modified $Sr_2NaNb_5O_{15}$-based [33] lead-free tungsten bronze relaxor ceramic, etc. Alternatively, sintering or post-annealing at a reducing atmosphere could also reduce the porosity and improve the electrical and energy storage properties [19].

4. Conclusions

The four compositions of tungsten bronze-type ceramics, i.e., $Ba_6Ti_2Nb_8O_{30}$ (BTN), $Ba_6Zr_2Nb_8O_{30}$ (BZN), $Sr_3TiNb_4O_{15}$ (STN), $Sr_3ZrNb_4O_{15}$ (SZN) are synthesized using the conventional mixed oxide route and systematically studied with a focus on their microstruc-

ture, dielectric response and its correlation with their temperature dependence of energy storage properties. Due to the different A and B site cations, those tungsten bronze ceramics show significantly different microstructure, permittivity response, and different extents of relaxor nature. All samples are porous, while STN has a relatively dense structure with inhomogeneous grains and SZN is most porous with connected irregular grains. It was also observed that BZN has the smallest grains with the range of 1 to 2 μm, while BTN and STN have inhomogeneous grain distribution with bigger grains up to 10 to 40 μm in size. Also, BTN, STN, and SZN are ferroelectric with diffused ferroelectric to paraelectric transition while BZN shows a strong relaxor feature with strong frequency dependence in permittivity. The dielectric loss values of those four ceramics from room temperature to 400 °C are all quite low compared with conventional ferroelectrics and thus promising for electronic industries. In addition, it was found that they generally have a low recoverable energy storage density (lower than 1 J/cm^3) due to their porous structure, especially SZN with an expected poorest energy storage response. Nevertheless, the energy storage properties show quite good temperature stability till 150 °C, demonstrating potential in high-temperature working environments.

Supplementary Materials: The following supporting information can be downloaded at: https://www.mdpi.com/article/10.3390/cryst13071073/s1, Figure S1: Tetragonal tungsten bronze (TTB) with tetragonal and orthorhombic unit cells indicated by dotted and dashed lines, respectively (a); structure of BTN (green, Blue, red, black atoms indicate Ba, Nb, O, Ti respectively); Table S1: EDS Result of the four tungsten bronze samples, i.e., BTN, BZN, STN and SZN; Figure S2: EDS Spectra of the four tungsten bronze samples, i.e., BTN(a), BZN(b), STN(c) and SZN(d); Figure S3: XRD raw data processed with Rietveld refinement of BZN (a), STN(b) and SZN (c) samples. Reference [34] are cited in the supplementary materials.

Author Contributions: Conceptualization, X.S. and N.H.K.; methodology, N.H.K.; software, X.S. and N.H.K.; validation X.S. and N.H.K. formal analysis, X.S. and N.H.K.; investigation, X.S. and N.H.K.; resources, X.S. and N.H.K.; data curation, X.S.; writing—original draft preparation, X.S.; writing—review and editing, N.H.K.; visualization, X.S. and N.H.K.; supervision, N.H.K.; project administration, N.H.K.; funding acquisition, X.S. and N.H.K. All authors have read and agreed to the published version of the manuscript.

Funding: This research was funded by Deutsche Forschungsgemeinschaft under KH 471/2 and the ETI-funding of Friedrich-Alexander-University Erlangen-Nürnberg.

Data Availability Statement: No extra data is available.

Conflicts of Interest: The authors declare no conflict of interest.

References

1. Zhang, X.; Ye, W.; Bu, X.; Zheng, P.; Li, L.; Wen, F.; Bai, W.; Zheng, L.; Zhang, Y. Remarkable capacitive performance in novel tungsten bronze ceramics. *Dalton Trans.* **2020**, *50*, 124–130. [CrossRef] [PubMed]
2. Li, Q.; Zhou, C.; Xu, J.; Yang, L.; Zhang, X.; Zeng, W.; Yuan, C.; Chen, G.; Rao, G. Tailoring antiferroelectricity with high energy-storage properties in $Bi_{0.5}Na_{0.5}TiO_3$–$BaTiO_3$ ceramics by modulating Bi/Na ratio. *J. Mater. Sci. Mater. Electron.* **2016**, *27*, 10810–10815.
3. Ogihara, H.; Randall, C.A.; Trolier-McKinstry, S. High-energy density capacitors utilizing $0.7BaTiO_3$–$0.3BiScO_3$ ceramics. *J. Am. Ceram. Soc.* **2009**, *92*, 1719–1724.
4. Yang, Z.; Du, H.; Qu, S.; Hou, Y.; Ma, H.; Wang, J.; Wang, J.; Wei, X.; Xu, Z. Significantly enhanced recoverable energy storage density in potassium–sodium niobate-based lead free ceramics. *J. Mater. Chem. A* **2016**, *4*, 13778–13785. [CrossRef]
5. Jamieson, P.; Abrahams, S.; Bernstein, J.L. Ferroelectric tungsten bronze-type crystal structures. I. Barium Strontium niobate $Ba_{0.27}Sr_{0.75}Nb_2O_5$. *J. Chem. Phys.* **1968**, *48*, 5048–5057.
6. Cao, L.; Yuan, Y.; Yang, Z.; Li, E.; Zhang, S. Crystal structure relaxor behaviors and energy storage performance of (Sr0.7Ba0.3)5LaNb7Ti3O30 tungsten bronze ceramics. *Ceram. Int.* **2019**, *46*, 6108–6114. [CrossRef]
7. Kim, M.-S.; Wang, P.; Lee, J.-H.; Kim, J.-J.; Lee, H.Y.; Cho, S.-H. Site Occupancy and Dielectric Characteristics of Strontium Barium Niobate Ceramics: Sr/Ba Ratio Dependence. *Jpn. J. Appl. Phys.* **2002**, *41*, 7042–7047. [CrossRef]
8. Jindal, S.; Vasishth, A.; Devi, S.; Anand, G. A review on tungsten bronze ferroelectric ceramics as electrically tunable devices. *Integr. Ferroelectr.* **2018**, *186*, 1–9. [CrossRef]

9. Simon, A.; Ravez, J. Solid-state chemistry and non-linear properties of tetragonal tungsten bronzes materials. *Comptes Rendus Chim.* **2006**, *9*, 1268–1276. [CrossRef]
10. Wang, B.-X.; Krogstad, M.J.; Zheng, H.; Osborn, R.; Rosenkranz, S.; Phelan, D. Active and passive defects in tetragonal tungsten bronze relaxor ferroelectrics. *J. Phys. Condens. Matter* **2022**, *34*, 405401. [CrossRef]
11. Whittle, T.A.; Lu, T.; Blanchard, P.; Hester, J.R.; Gu, Q.; Liu, Y.; Schmid, S. Synthesis, structure and dielectric properties of the $Sr_3Ti_1-xZr_xNb_4O_{15}$, ($0 \leq x \leq 1$), series of tungsten bronze type compounds. *CrystEngComm* **2020**, *22*, 4994–5001.
12. Chen, G.-H.; Qi, B. Effect of CASP glass doping on sintering and dielectric properties of SBN ceramics. *J. Alloy. Compd.* **2009**, *473*, 414–417. [CrossRef]
13. Zhang, S.T.; Yuan, G.; Chen, J.; Gu, Z.B.; Yang, B.; Yin, J.; Cao, W. Structural evolving sequence and porous $Ba_6Zr_2Nb_8O_{30}$ ferroelectric ceramics with ultrahigh breakdown field and zero strain. *J. Am. Ceram. Soc.* **2013**, *96*, 555–560.
14. Bai, H.; Li, J.; Wu, Y.; Hong, Y.; Shi, K.; Zhou, Z. Exploring determinants of lattice structure and high energy storage properties of Fe-doped SBN ceramics. *Ceram. Int.* **2019**, *45*, 11109–11113. [CrossRef]
15. Stephenson, N.C. The crystal structure of the tetragonal bronze, $Ba_6Ti_2Nb_8O_{30}$. *Acta Crystallogr.* **1965**, *18*, 496–501. [CrossRef]
16. Jiang, D.; Ekren, D.; Azough, F.; Day, S.J.; Chen, K.; Mahajan, A.; Kepaptsoglou, D.M.; Ramasse, Q.M.; Reece, M.J.; Freer, R. The structure and thermoelectric properties of tungsten bronze $Ba_6Ti_2Nb_8O_{30}$. *J. Appl. Phys.* **2019**, *126*, 125115.
17. Roberts, G.; Cava, R.; Peck, W.; Krajewski, J. Dielectric properties of barium titanium niobates. *J. Mater. Res.* **1997**, *12*, 526–530.
18. Itoh, Y.; Iwasaki, H. Ferroelectric and optical properties of $Ba_6Ti_2Nb_8O_{30}$ single crystals. *J. Phys. Chem. Solids* **1973**, *34*, 1639–1645. [CrossRef]
19. Massarotti, V.; Capsoni, D.; Bini, M.; Azzoni, C.B.; Mozzati, M.C.; Galinetto, P.; Chiodelli, G. Structural and Spectroscopic Properties of Pure and Doped $Ba_6Ti_2Nb_8O_{30}$ Tungsten Bronze. *Cheminform* **2006**, *37*, 17798–17805. [CrossRef]
20. He, Q.; Schmid, S.; Chen, X.; Peng, B.; Li, C.; Hu, C.; Liu, L.; Hinterstein, M. Structure and relaxor ferroelectric behavior of the novel tungsten bronze type ceramic $Sr_5BiTi_3Nb_7O_{30}$. *J. Appl. Phys.* **2022**, *131*, 164102.
21. Chi, E.O.; Gandini, A.; Ok, K.M.; Zhang, L.; Halasyamani, P.S. Syntheses, structures, second-harmonic generating, and ferroelectric properties of tungsten bronzes: A6M2M '8O30 (A= Sr^{2+}, Ba^{2+}, or Pb^{2+}; M= Ti^{4+}, Zr^{4+}, or Hf^{4+}; M '= Nb^{5+} or Ta^{5+}). *Chem. Mater.* **2004**, *16*, 3616–3622.
22. Neurgaonkar, R.; Nelson, J.; Oliver, J. Ferroelectric properties of the tungsten bronze M2+6M4+2Nb_8O_{30} solid solution systems. *Mater. Res. Bull.* **1992**, *27*, 677–684. [CrossRef]
23. Jiang, D. Tungsten Bronze Structured Compounds for Thermoelectric Applications. Ph.D. Thesis, The University of Manchester, Manchester, UK, 2019.
24. Rao, K.S.; Subrahmanyam, A.S.V.; Viswarupachary, P. Microstructural and anomalous resistivity behavior of modified ferroelectric $Ba_6Ti_2Nb_8O_{30}$. *Ferroelectrics* **1998**, *215*, 95–102. [CrossRef]
25. Yuan, Y.; Chen, X.M.; Wu, Y.J. Diffused ferroelectrics of $Ba_6Ti_2Nb_8O_3$ and $Br_6Ti_2Nb_8O_3$ with filled tungsten-bronze structure. *J. Appl. Phys.* **2005**, *98*, 084110. [CrossRef]
26. Xie, R.J.; Akimune, Y.; Matsuo, K.; Sugiyama, T.; Hirosaki, N.; Sekiya, T. Dielectric and ferroelectric properties of tetragonal tungsten bronze $Sr_2-xCa_xNaNb_5O_{15}$ (x= 0.05–0.35) ceramics. *Appl. Phys. Lett.* **2002**, *80*, 835–837.
27. Bendahhou, A.; Marchet, P.; El-Houssaine, A.; El Barkany, S.; Abou-Salama, M. Relationship between structural and dielectric properties of Zn-substituted Ba5CaTi2−xZnxNb8O30 tetragonal tungsten bronze. *CrystEngComm* **2021**, *23*, 163–173.
28. Parida, B.; Das, P.R.; Padhee, R.; Choudhary, R. Phase transition and conduction mechanism of rare earth based tungsten-bronze compounds. *J. Alloy. Compd.* **2012**, *540*, 267–274. [CrossRef]
29. Das, P.R.; Biswal, L.; Behera, B.; Choudhary, R.N.P. Structural and electrical properties of Na2Pb2Eu2W2Ti4X4O30 (X= Nb, Ta) ferroelectric ceramics. *Mater. Res. Bull.* **2009**, *44*, 1214–1218.
30. Zhang, X.; Wang, H.; Bu, X.; Zheng, P.; Li, L.; Wen, F.; Bai, W.; Zhang, J.; Zheng, L.; Zhai, J.; et al. Simultaneously Realizing Superior Energy Storage Properties and Outstanding Charge–Discharge Performances in Tungsten Bronze-Based Ceramic for Capacitor Applications. *Inorg. Chem.* **2021**, *60*, 6559–6568. [CrossRef] [PubMed]
31. Xu, S.; Shen, S.; Hao, R.; Peng, Z.; Zhang, F.; Wu, D.; Liang, P.; Chao, X.; Wei, L.; Yang, Z. Relaxor nature and superior energy storage performance of Sr2Ag0.2Na0.8Nb5O15-based tungsten bronze ceramics through B-site substitution. *Chem. Eng. J.* **2021**, *433*, 133812. [CrossRef]
32. Yang, B.; Zhang, J.; Lou, X.; Gao, Y.; Shi, P.; Yang, Y.; Yang, M.; Cui, J.; Wei, L.; Sun, S. Interfaces, Enhancing Comprehensive Energy Storage Properties in Tungsten Bronze $Sr_{0.53}Ba_{0.47}Nb_2O_6$-Based Lead-free Ceramics by B-Site Doping and Relaxor Tuning. *ACS Appl. Mater.* **2022**, *14*, 34855–34866.
33. Xu, S.; Hao, R.; Yan, Z.; Hou, S.; Peng, Z.; Wu, D.; Liang, P.; Chao, X.; Wei, L.; Yang, Z. Enhanced energy storage properties and superior thermal stability in SNN-based tungsten bronze ceramics through substitution strategy. *J. Eur. Ceram. Soc.* **2022**, *42*, 2781–2788. [CrossRef]
34. Scott, J. Ferroelectric Relaxor Quantum Crystals. *J. Cryst.* **2018**, *8*, 180.